APPLIED PHYSICS

A flexoelectricity-enabled ultrahigh piezoelectric effect of a polymeric composite foam as a strain-gradient electric generator

Dongze Yan[1], Jianxiang Wang[2,3], Jinwu Xiang[1], Yufeng Xing[1], Li-Hua Shao[1]*

All dielectric materials including ceramics, semiconductors, biomaterials, and polymers have the property of flexoelectricity, which opens a fertile avenue to sensing, actuation, and energy harvesting by a broad range of materials. However, the flexoelectricity of solids is weak at the macroscale. Here, we achieve an ultrahigh flexoelectric effect via a composite foam based on PDMS and CCTO nanoparticles. The mass- and deformability-specific flexoelectricity of the foam exceeds 10,000 times that of the solid matrix under compression, yielding a density-specific equivalent piezoelectric coefficient 120 times that of PZT. The flexoelectricity output remains stable in 1,000,000 deformation cycles, and a portable sample can power LEDs and charge mobile phones and Bluetooth headsets. Our work provides a route to exploiting flexible and light-weight materials with highly sensitive omnidirectional electromechanical coupling that have applications in sensing, actuation, and scalable energy harvesting.

INTRODUCTION

Flexoelectricity refers to generation of electricity by materials when subjected to nonuniform mechanical strains such as bending and twisting (*1–5*). Compared to piezoelectricity, flexoelectricity is a universal effect not limited by crystalline symmetry, polarization, and depolarization temperature, and is thus allowed in all dielectric materials including soft matters such as polymers (*6–9*), biomaterials (*10–13*), and liquid crystals (*2, 14, 15*), as well as ceramics and semiconductors (*16*) and perovskites under high temperatures (*17*). The flexoelectric effect finds wide applications in flexoelectronics (*18*), sensing and actuating (*19–21*), photoflexoelectricity (*22*), data storage (*23*), and energy harvesting (*24–26*). Photocurrent of ferroelectric oxides can be enhanced by two orders of magnitude by the flexoelectric effect corresponding to a giant strain gradient as high as 10^7/m (*27*), and the bulk photovoltaic coefficient of MoS_2 sheets is enhanced by orders of magnitude compared to that of most noncentrosymmetric materials under a strain gradient of 10^6/m (*28*). Photoconductance of $BiFeO_3$ films can be effectively mediated by strain gradients (*29, 30*). However, the flexoelectric effect is size dependent and is weak at the macroscale, as is evident from the small flexoelectric coefficients in the range of 10^{-5} to 10^{-3} C/m for ferroelectrics and ceramics and 10^{-10} to 10^{-8} C/m for polymers (*31*). Thus, hereto, the effect has been mostly investigated and used at nano- to microscales where local giant strain gradients can be realized by various ways such as indentation (*32–34*), lattice mismatch (*27, 30, 35–38*), and bending of nano/microscale beams (*26, 39–42*).

In this work, we achieve an ultrahigh flexoelectric effect through design of a composite foam based on polydimethylsiloxane (PDMS) and a twisted foam structure (Fig. 1). The mass- and deformability-specific flexoelectric response of the structure is more than 10,000 times that of the solid truncated pyramid PDMS material under compression. The foam structure can generate electricity under omnidirectional deformation and thus can also be used as a piezoelectric material. In this sense, the equivalent piezoelectric coefficient (1522 pC/N) is comparable to the high-performance piezoelectric ceramic $Pb(Mg_{1/3}Nb_{2/3})O_3$-$PbTiO_3$ (PMN-PT, 1510 pC/N), yielding a 120 times higher density-specific equivalent piezoelectric coefficient than lead-zirconate-titanate (PZT). By this design, we generate an output of electricity at the microampere scale with a simple portable device. We term this device a "strain-gradient electric generator." By storing energy generated by the foam samples, we have successfully lit red light-emitting diode (LED) lights and charged mobile phones and Bluetooth headsets. The output remains stable over 1 million deformation cycles.

RESULTS

Fabrication and characterization of structured composite foam

PDMS is one of the most commonly used soft elastomers in flexible electronics, biomedical devices, and energy harvesting because of its large reversible deformation, low cost, and excellent biocompatibility (*43*). However, the flexoelectric coefficient of PDMS is quite low at 10^{-10} C/m (*8, 42*). To enhance the flexoelectric output of PDMS, ceramic particles of copper-calcium-titanate ($CaCu_3Ti_4O_{12}$; CCTO) were added into the PDMS matrix to make a composite (Fig. 1A). The CCTO particles of nanoscale (n-CCTO) and microscale diameter (μ-CCTO) were used since it has been reported that dielectric permittivity of CCTO increases with decreasing particle size (*44*). CCTO exhibits high "effective" dielectric permittivity (10^5 to 10^4 at room temperature) due to the barrier-layer mechanism (*44, 45*). Narvaez *et al.* (*16*) have shown that an oxide semiconductor heterostructure exhibits an enhanced flexoelectric-like response because of the barrier-layer mechanism. In addition, the piezoelectric effect is excluded because the CCTO particles have a centrosymmetric structure (*46*). The dielectric permittivity of the

[1]School of Aeronautic Science and Engineering, Beihang University, Beijing 100191, P.R. China. [2]State Key Laboratory for Turbulence and Complex System, Department of Mechanics and Engineering Science, College of Engineering, Peking University, Beijing 100871, P.R. China. [3]CAPT-HEDPS and IFSA Collaborative Innovation Center of MoE, College of Engineering, Peking University, Beijing 100871, P.R. China.
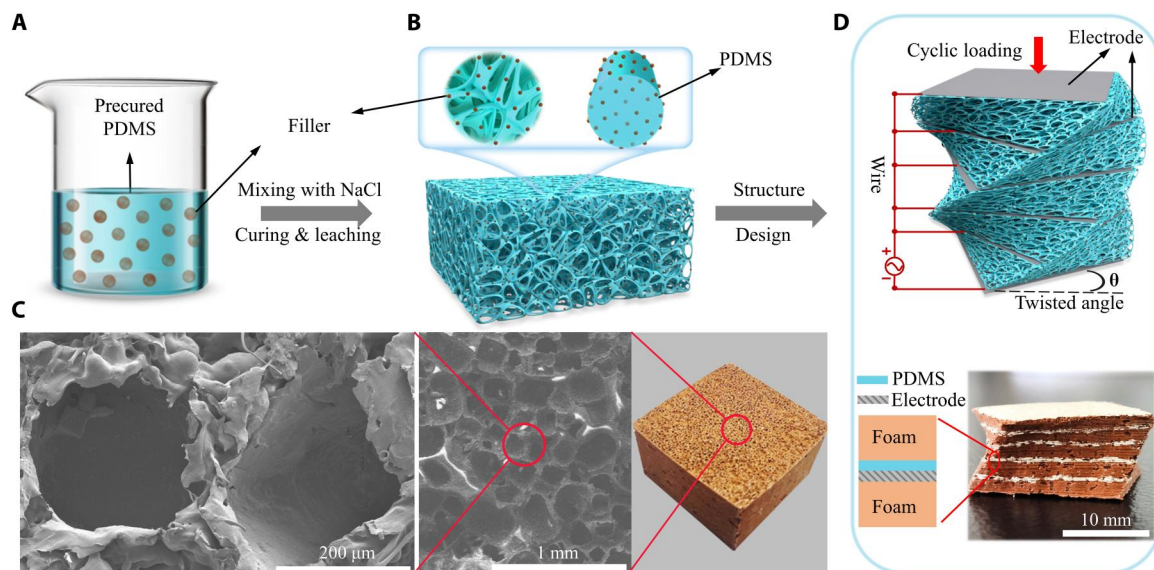*Corresponding author. Email: shaolihua@buaa.edu.cn

Fig. 1. Fabrication and characterization of twisted composite foam. Schematic plots of precured PDMS and n-CCTO particle mixture (**A**) and composite foam with ligaments consisting of PDMS matrix and n-CCTO particles (**B**). (**C**) Photo and SEM images of the foam structure. (**D**) Twisted PDMS-CCTO composite foam and configuration of electrodes.

solid PDMS/CCTO composite is theoretically analyzed in the "Dielectric permittivity of solid composite" section of Materials and Methods, and it is shown (fig. S1) that the dielectric permittivity of the binary composite increases with increasing dielectric permittivity and volume fraction of the filler.

Then, a foam structure was fabricated with the composite of PDMS/n-CCTO as the base material, as schematically illustrated in Fig. 1B (details of the fabrication process can be found in the "Fabrication" section of Materials and Methods). The scanning electron microscopy (SEM) images and a photo of the foam structure are shown in Fig. 1C, where the randomly distributed open pores and ligaments at several tens of micrometers can be observed. Because of the disordered arrangement in all directions, the internal ligaments of the foam structure can undergo bending deformation when a block of the foam is subjected to any loading and thus generate electricity. The aspect ratio l/δ (l and δ are the pore diameter and ligament thickness of the foam structure, respectively) of the ligaments can be optimized by adjusting the fractions of PDMS and sacrificial NaCl particle template to create large strain gradients. When the foam is subjected to cyclic compression, the effective flexoelectric current $I^{\star}$ can be described by the scaling law

$$I^{*} \propto \alpha \mu f \lambda_{\mathrm{pp}} n^{*}\left(\frac{l}{\delta}\right) \qquad (1)$$

where α, μ, f, λ_{pp}, and $n^{\star}$ are a nondimensional parameter related to the geometry of the microstructure, the flexoelectric coefficient of the solid (i.e., the ligaments), the frequency of the cyclic deformation, the compression displacement, and the total number of layers where the charges are collected, respectively (8). Therefore, to create high strain gradients and to collect more electricity, in this work, we devise a composite foam with an optimum aspect ratio of the ligaments. The thickness of the ligaments decreases with an increase of mass ratio m (fig. S2A), defined as the ratio of the mass of the sacrificial NaCl particle template to that of PDMS. As described in the

"Calculation of mass ratio" section of Materials and Methods and fig. S2B, the flexoelectric current of the samples with $m = 6$ is the largest, which is selected here (aspect ratio is ca. 4.5). The relative dielectric permittivity and dielectric loss of the PDMS foam are 0.92 and 0.005, respectively, as shown in fig. S3A. The relative dielectric permittivity of the PDMS/n-CCTO$_{v=5\%}$ (the volume fraction of n-CCTO is $v = 5\%$) foam is 4.29, with a low dielectric loss of 0.009, as shown in fig. S3B.

In addition to choosing an optimized aspect ratio of the ligaments, we have designed a five-layer stacked-and-twisted composite foam structure with a coupled compression-torsion deformation mode, which will twist under unidirectional compression, as shown in Fig. 1D. The top and bottom surfaces of the foam structure were each coated with a conductive electrode. In addition, four electrodes were embedded inside the structure, with the top layer of each electrode insulated with a thin layer of PDMS, as schematically shown in the inset of Fig. 1D. The wires connecting the electrode on the top surface of the foam structure and the four internal electrodes were connected together to the input channel of the current amplifier, and the electrode on the bottom of the foam structure was connected to the grounded input channel (Fig. 1D).

The deformations of the internal ligaments of the nontwisted and twisted foam structures were calculated by the finite element analysis software ABAQUS based on the unit cell of the Gibson-Ashby (G-A) model (47), shown in Fig. 2. For both the nontwisted (Fig. 2A) and twisted (Fig. 2B) foam structures, most of the ligaments undergo bending deformation under compression. However, the twisted foam structure has a coupled compression-torsion deformation mode, i.e., it twists under unidirectional compression. Thus, the internal ligaments undergo both torsional and bending deformations, as shown in Fig. 2B, and the strains of the ligaments are much larger than those of the straight ones in Fig. 2A. The strain nephograms of the cross sections of the horizontal ligaments in both the nontwisted and twisted unit cells are given
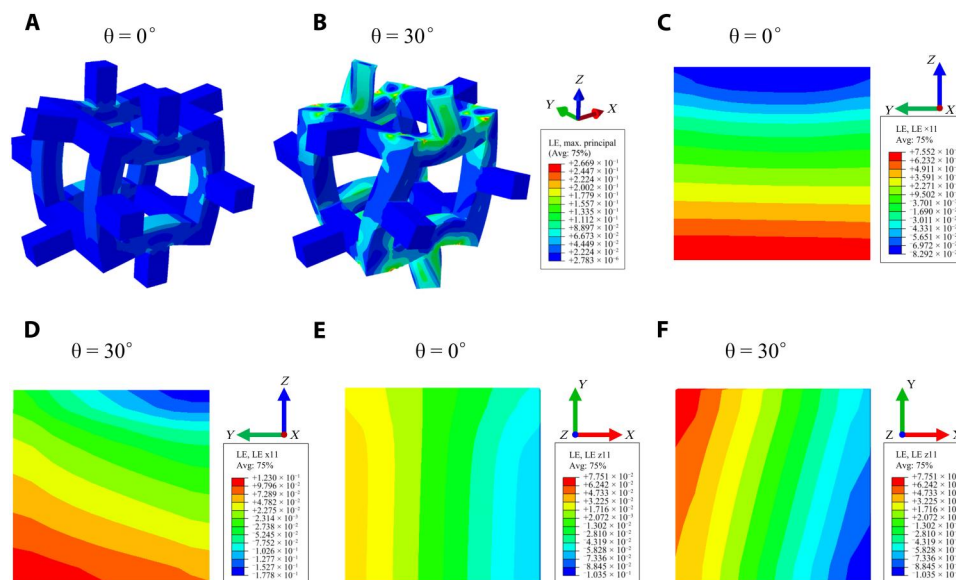
Fig. 2. Deformation of nontwisted and twisted structures under compression based on the finite element analysis. Strain nephograms for the nontwisted G-A model (**A**) and for the twisted G-A model (**B**). Nephograms (**C**) (nontwisted) and (**D**) (twisted) show the variations of the axial strains in the transverse direction (*Z* direction) for the horizontal beams and (**E**) (nontwisted) and (**F**) (twisted) show the variations of the axial strains in the transverse direction (*X* direction) for the vertical beams.

in Fig. 2 (C and D) with the maximum strains of 8.3 and 17.8%, respectively. The strain nephograms of the cross sections of the vertical ligaments in both the nontwisted and twisted unit cells are given in Fig. 2 (E and F) with the maximum strains of 7.6 and 10.4%, respectively. The corresponding strain gradients ($\varepsilon_{xx,z}$) of the horizontal ligaments in the nontwisted and twisted unit cells are 3160/m and 6000/m, respectively. The strain gradients ($\varepsilon_{zz,x}$) of the vertical ligaments of the nontwisted and twisted unit cells are 2540/m and 3620/m, respectively. For this reason, we have chosen to focus on the performance of the stacked-and-twisted macrostructure with a relative twisting angle θ = 30° between the top and bottom surfaces of the sample, as shown in Fig. 1D.

Before we present the performance of the stacked-and-twisted foam sample of Fig. 1D, we give a detailed description of the three contributions that lead to the enhancement of the flexoelectric performance of the stacked-and-twisted composite foam. These three contributions come from the composite structure (compared to pure PDMS), the stacking, and the twisting.

First, strontium titanate (STO) and α-cristobalite particles were also used to make composites. These particles have a centrosymmetric structure (*48, 49*), and their dielectric permittivities ε′ are ca. 350 (*50*) and ca. 3 (*51*), respectively. The particle sizes of n-CCTO, STO, and α-cristobalite particles are similar. Flexoelectric coefficients of pure PDMS and the PDMS/α-cristobalite composite solid beams are shown in Fig. 3A. The pure PDMS and the composites with 5 or 10% volume fractions of α-cristobalite particles have similar flexoelectric coefficients. Figure 3B shows the effective flexoelectric currents of the nontwisted and nonstacked composite foams made of the PDMS matrix filled with four kinds of particles (α-cristobalite, STO, nanoscale n-CCTO, and microscale μ-CCTO) with different volume fractions as functions of macroscopic unidirectional compression strain. It is seen that nanoscale n-CCTO with a high volume fraction and high effective dielectric permittivity generates the highest effective flexoelectric current. The flexoelectric current

of the PDMS/n-CCTO$_{v=5\%}$ foam is nearly 10 times larger than that of the pure PDMS foam.

Second, for a stacked foam structure of *n* layers, as described above, the flexoelectric current, I_n, is approximately equal to *nI*, where *I* is the flexoelectric current of one layer. Figure 3C shows that the flexoelectric current increases almost linearly with the number *n* of layers for *n* = 1, 2, and 3. Similar methods have also been reported in the literature to increase the output of piezoelectricity (*52–55*). Previous experiment of Kwon *et al.* (*56*) for the flexoelectricity of multilayered barium strontium titanate cantilever beams under bending also demonstrates that the flexoelectricity output "is proportional to the number of flexoelectric layers."

Last, the flexoelectric currents of the twisted three-layer PDMS/n-CCTO$_{v=5\%}$ foam structure with relative twisting angles (θ) 0°, 10°, 20°, and 30° under unidirectional compression are shown in Fig. 3D. The flexoelectric current increases with an increase in the relative twisting angle. The flexoelectric current of the sample with θ = 30° is ca. two times larger than that of the nontwisted one.

Performance of stacked-and-twisted composite foam

We now investigate the performance of the stacked-and-twisted (θ = 30°, five layers) PDMS/n-CCTO$_{v=5\%}$ composite foam structure with macroscopic dimensions of 2 cm by 2 cm by 1 cm. The flexoelectric current under unidirectional compression, which is ca. two times larger than that of the nontwisted one, is shown in Fig. 4A. Figure 4B shows variations of the flexoelectric current (left vertical axis) and the macroscopic applied displacement (right vertical axis) versus time, which demonstrates synchronicity of the flexoelectric response and applied compression. The dependence of the flexoelectric current on the loading frequency is shown in Fig. 4C. The flexoelectric current increases linearly with loading frequency below 5 Hz but then the current starts to decrease. All the measurements given below are based on *f* = 2 Hz. Figure 4D shows that flexoelectric current is stable under continuous cyclic compression for more
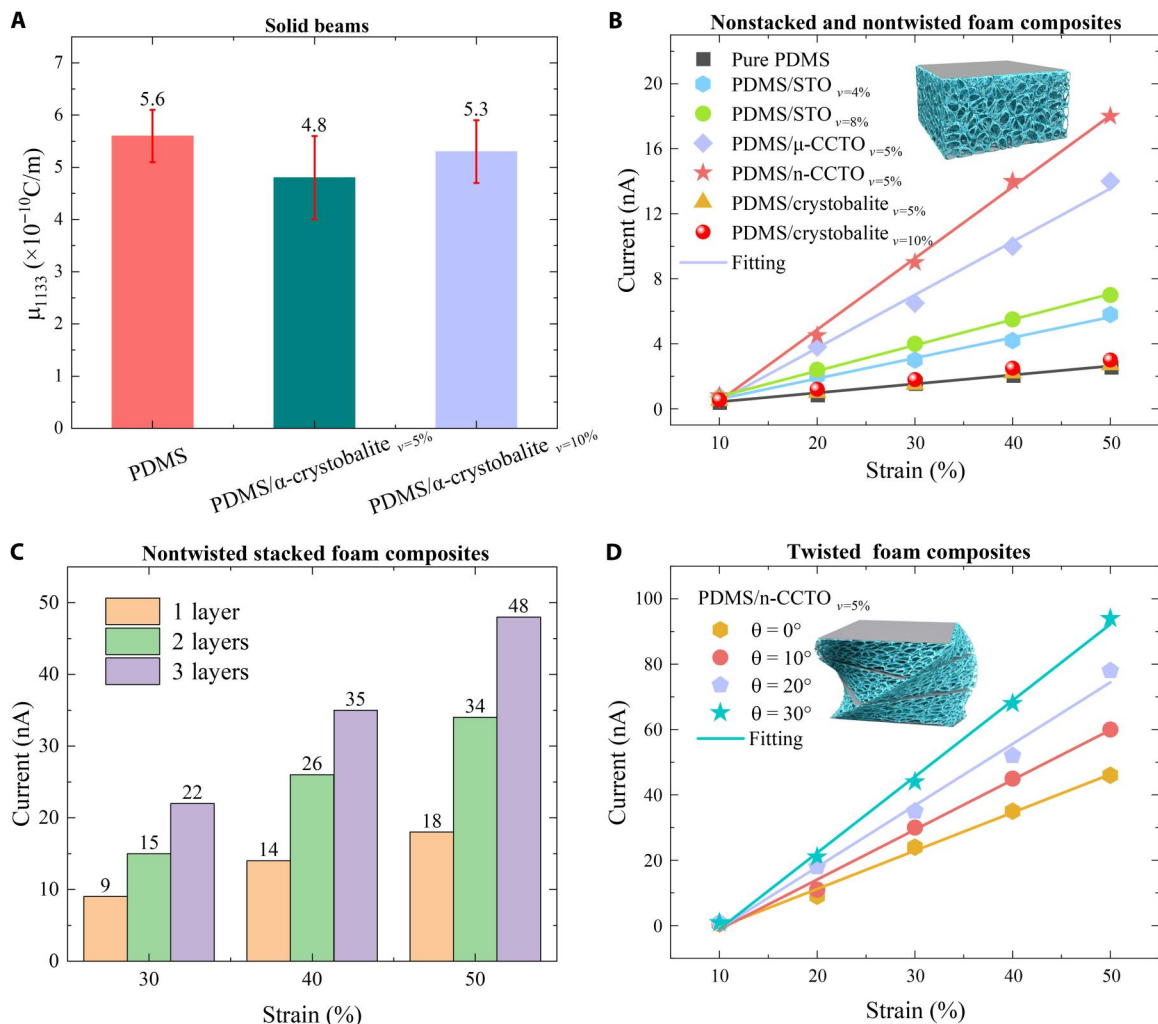
Fig. 3. Performance of solids and foams. (**A**) Flexoelectric coefficients of pure PDMS and PDMS/α-cristobalite composite solid beams. (**B**) Flexoelectric currents of the nontwisted and nonstacked composite foam based on PDMS matrix filled with four kinds of particle (α-cristobalite, STO, n-CCTO, and μ-CCTO) with different volume fractions as functions of macroscopic compression strain. (**C**) Flexoelectric currents of the nontwisted stacked foam PDMS/n-CCTO$_{v=5\%}$ with different numbers of layers. (**D**) Flexoelectric currents of twisted three-layer PDMS/n-CCTO$_{v=5\%}$ foams with different twist angles θ.

than 1 hour without any deterioration in the mechanical behavior of the composite foam (Fig. 4E). This proves reproducibility of the stress-strain curves over 1,000,000 loading-unloading cycles. The flexoelectric output with peak current of 130 ± 10 nA and equivalent compressive modulus $(43 \pm 1.5) \times 10^{-3}$ MPa remain stable for 60 days, as shown in Fig. 4F.

The mass- and deformability-specific flexoelectric current is defined as $W_{sec} = I_{max}/(m_g \varepsilon)$, where I_{max}, m_g, and ε represent the maximum flexoelectric current, mass of the sample, and applied unidirectional compression strain, respectively. Our sample (stacked-and-twisted PDMS/n-CCTO$_{v=5\%}$ with dimensions of 2 cm by 2 cm by 1 cm) has an ultrahigh specific flexoelectric output of $W_{sec} = 1400$ pA g^{-1} %$^{-1}$, which is four orders of magnitude larger than that of the solid truncated pyramid PDMS (0.13 pA g^{-1} %$^{-1}$) under unidirectional compression (comparison shown in Fig. 5A) and two orders of magnitude larger than that of pure PDMS foam without the nanoparticles and optimized structures ([8]). Conventionally, the piezoelectric effect is the most commonly

exploited charge-load coupling effect in various devices in engineering. An important figure of merit of a piezoelectric material is the longitudinal piezoelectric coefficient d_{33}, which is the charge polarized per load. Here, the equivalent charge-load coupling coefficient, d_{33}^{eq}, of the foam sample is calculated according to the equation

$$d_{33}^{eq} = \frac{dQ}{dF} = \frac{d\left(\frac{i}{2\pi f}\right)}{d(E\varepsilon A)} = \frac{1}{2\pi f E A}\frac{di}{d\varepsilon} \tag{2}$$

where i, ε, f, E, and A are the flexoelectric current, compressive strain, frequency of cyclically applied load, equivalent compressive modulus, and cross-sectional area of the sample, respectively. d_{33}^{eq} of the PDMS/n-CCTO$_{v=5\%}$ sample is 1522 pC/N, which is considerably larger than that of the most commonly used piezoelectric ceramics ([57]–[64]), as shown in Fig. 5B. d_{33}^{eq} of our polymeric composite foam is larger than that of the lead-free piezoelectric ceramics and is comparable to that of known lead-containing piezoelectric ceramics
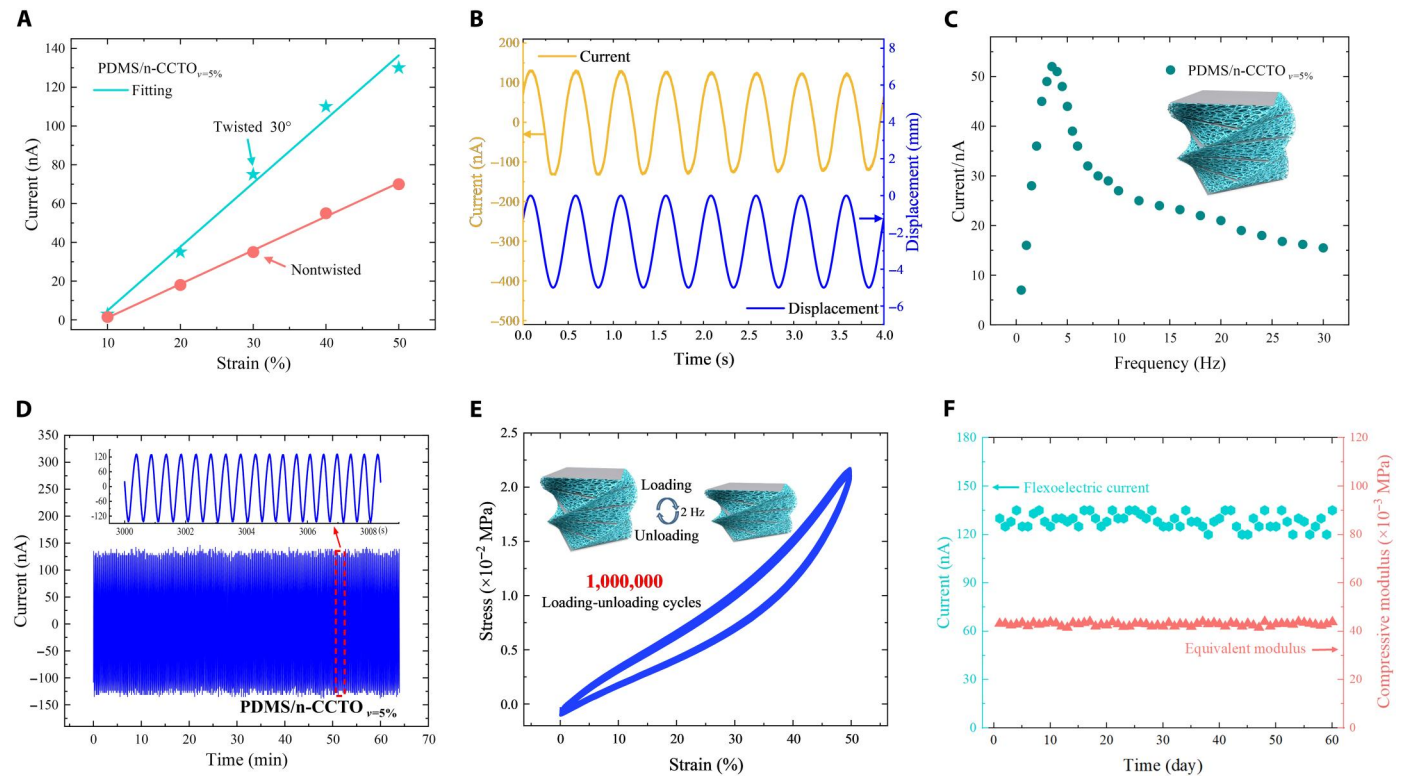
Fig. 4. Flexoelectric currents and mechanical property of stacked-and-twisted PDMS/n-CCTO$_{v=5\%}$ foam (θ = 30°, five layers). (**A**) Comparison of flexoelectric currents of the twisted and nontwisted samples. (**B**) Flexoelectric current (left axis, yellow) and the applied displacement (right axis, blue). (**C**) Dependence of the flexoelectric current on the loading frequency at 20% applied strain. (**D**) Stable flexoelectric current with continuous measurement for more than 1 hour. (**E**) Reproducible stress-strain curves over 1,000,000 loading-unloading cycles. (**F**) Flexoelectric peak current (left axis, green) and equivalent compressive modulus (right axis, pink) of the foam over 60 days (measurements were made for 10 min each day over 60 days at ε = 50%).

[e.g., PMN-PT (*64*)]. The flexoelectric output of the composite foam can be further improved by using larger volume fractions of fillers with higher dielectric permittivity. Moreover, one of the major advantages of the foam is its light weight. The density of the foam is ca. 250 kg/m³, whereas the density of the piezoelectric ceramics is ca. 6800 to 8500 kg/m³. The density-specific equivalent charge-load coupling coefficient d_{33}^{eq} of the foam is compared with those of typical high-performance piezoelectric polymer and ceramics in Fig. 5C: The density-specific d_{33}^{eq} of PDMS/n-CCTO$_{v=5\%}$ is 120 times and 380 times larger than that of the most commonly used PZT ceramic and β-polyvinylidene difluoride polymer, respectively. The PDMS/n-CCTO$_{v=5\%}$ foam has an extremely long working life with peak current output remaining stable for more than 1,000,000 continuous cycles, as shown in Fig. 5D.

The universality of flexoelectricity effect provides a promising route to direct conversion of ambient mechanical energy into electricity. Thus, attempts have been made to design energy harvesters based on flexoelectricity (*24–26*, *65*). Because of the need for large strain gradients, previous flexoelectric energy harvesters are based on beam or plate bending (*24–26*, *65*). The weak flexoelectric output of solids has, however, hindered the development of energy harvesting based on flexoelectricity. Thus, practical and scalable energy harvesting based on flexoelectricity is yet to be realized. While the piezoelectric (*66*, *67*) and triboelectric (*68*, *69*) nanogenerators and flexoelectric energy harvesters at the nano/microscale are good energy sources for micro/nanoscale devices (*24*, *26*, *66*),

everyday portable devices call for generators that are easily scalable, cost effective, durable, and adaptable to wide application scenarios.

The ultrahigh flexoelectric output of the composite foam enables it to convert natural mechanical energy into electric energy easily as a strain gradient electric generator. The flexoelectric output voltage and current of the PDMS/n-CCTO$_{v=5\%}$ foam sample (2 cm by 2 cm by 1 cm) are 1.85 V and 130 nA, respectively, which charges a capacitor (4.7 μF) to 1.8 V in 2 min under cyclic compression. Then, the charged capacitor lights up a commercial LED as the inset of Fig. 5D shows (movie S1).

The PDMS/n-CCTO$_{v=5\%}$ foam was fabricated into an insole and placed in a sports shoe, enabling mechanical deformation energy to be directly converted into electricity during walking. The peak electric output voltage and current of an insole (size, 200 cm² by 0.75 cm) are 5.8 V and 1.0 μA, respectively, as shown in the inset of Fig. 5E. The insole was connected directly to a capacitor (4 mF) during walking at ca. 2 Hz. The flexoelectricity generated during a 7-hour walk charged the capacitor to 5.8 V, which then realized charging a smart phone, and charged a Bluetooth headset for a period of ca. 2 s (Fig. 5E and movie S1).

In addition to harvesting energy on land, the foam structure could be used to harvest energy from vibrations like tidal motion. Here, the foam is pasted on the inner wall of a 16-cm-diameter ball containing an inertial block (diameter, 8 cm) in the middle. The vibration causes relative movement between the ball and the inertial block to produce displacement, which deforms the foam. The
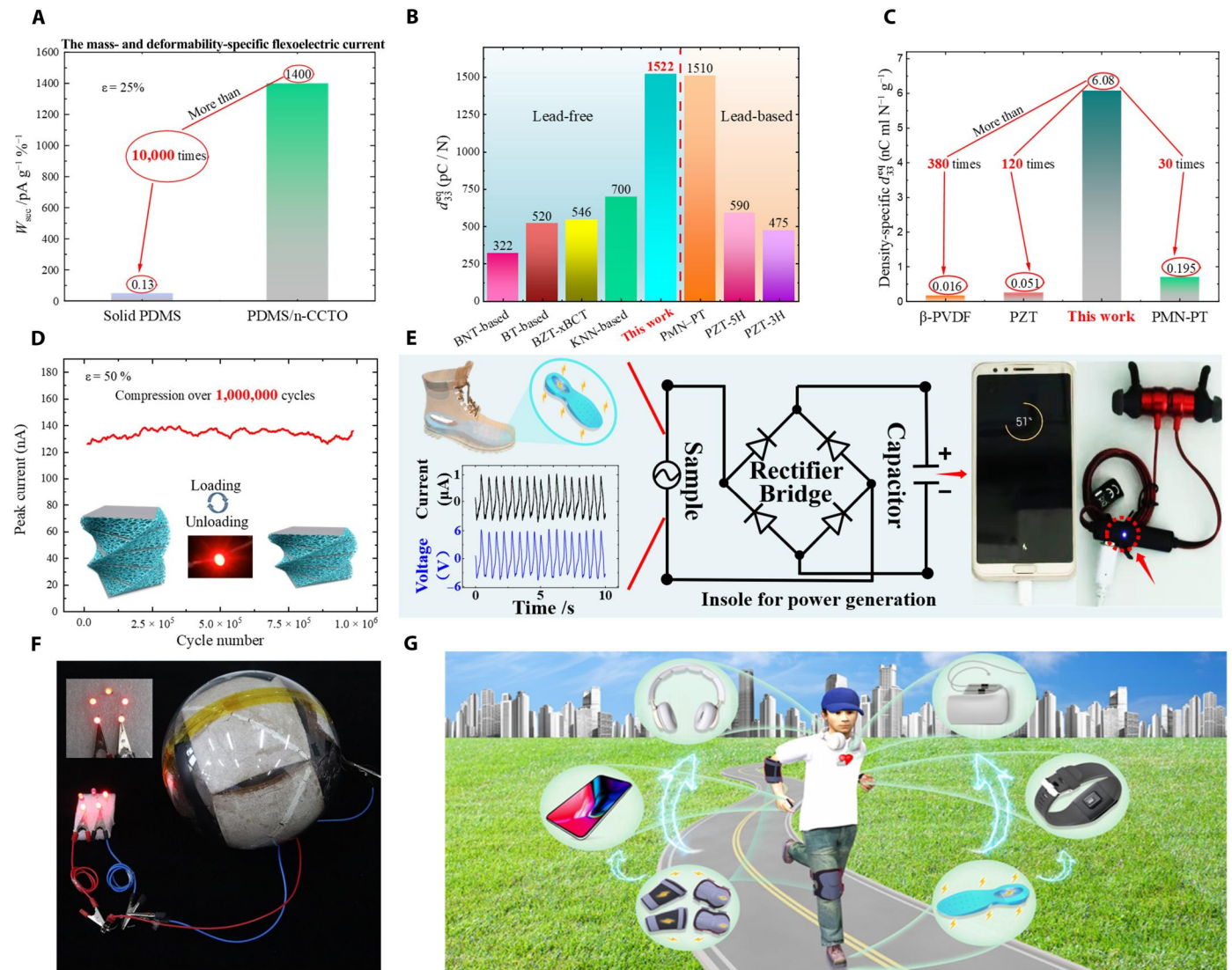
Fig. 5. Performance and applications of strain gradient electric generators based on microstructured polymeric composite. (**A**) Comparison of the mass- and deformability-specific flexoelectric current W_{sec} between twisted PDMS/n-CCTO$_{v=5\%}$ foam and solid truncated pyramid PDMS under an applied strain of 25%, which shows that the former is four orders of magnitude larger than that of the latter. (**B**) Comparison of equivalent piezoelectric coefficients and (**C**) comparison of density-specific equivalent piezoelectric coefficients, between PDMS/n-CCTO$_{v=5\%}$ foam sample with dimensions 2 cm by 2 cm by 1 cm and common piezoelectric materials. (**D**) Peak current over 1,000,000 cycles of compression of the composite foam generator, whose output flexoelectricity charges a capacitor, which can then light LEDs (red LED, forward rated voltage and current are 1.8 V and 20 mA), shown in the inset. (**E**) Flexoelectricity (the current and voltage are shown in the inset) generated by one insole during walking motion charges the capacitor, which can then charge a smart phone and Bluetooth headset. (**F**) A ball with the foam inside when subjected to vibration charges a capacitor, which can then light up five commercial LEDs. (**G**) Potential applications of wearable strain gradient generators such as insoles, protective ankle, and knee pads, to power other wearable devices.

vibration is simulated by manually shaking the ball (at ca. 3 Hz), and the induced peak current and voltage are 8 ± 2 µA and 11 ± 2 V, respectively, capable of charging a capacitor (22 µF) to 10 V in ca. 40 s. The capacitor can light up five commercial LEDs, as shown in Fig. 5F and movie S2.

To date, only the flexoelectricity generated by the ligaments near the conductive electrode has been harvested. In the future, all of the fine ligaments can be coated with electrodes at desired locations to contribute to the flexoelectricity output by more ingenious design and fabrication technology, similar to three-dimensional (3D) printing and other additive manufacturing technologies.

Theoretically (see the "Flexoelectric output of an ideal microstructured insole" section of Materials and Methods), a pair of insoles each of size 200 cm² by 1 cm, containing 0.5-µm-thick ligaments can generate peak flexoelectric voltage reaching 10 V at a walking frequency of 1 Hz with the peak output current reaching 10 A. In this manner, the instantaneous peak power generated by each step of one foam insole can reach 100 W. This power is enough to charge immediately smart devices, such as pacemakers, sport watches, mobile phones, and so on. It will take ca. 167 s to fully charge a 400-mA·hour Bluetooth headset battery and ca. 27 min to fully charge a 4000-mA·hour phone battery. Owing to their high

flexibility, durability, and ease of manufacture, light-weight polymeric foam structures with an ultrahigh flexoelectric output can be easily made as protective ankle and knee pad wearable generators to power other wearable devices (Fig. 5G).

DISCUSSION

In summary, we have realized practical flexoelectricity harvesting at the macroscopic scale via a polymeric composite foam with an ultrahigh flexoelectric effect. The mass- and deformability-specific flexoelectric output is 10,000 times that of the pure solid polymer under unidirectional compression. The foam can also be used as a light-weight and sensitive piezoelectric material with its ultrahigh equivalent piezoelectric coefficient. The electric output remains stable over 1,000,000 cyclic deformations. Owing to its omnidirectional mechanoelectric coupling (the flexoelectric effects under macroscopic bending are demonstrated in the "Flexoelectric effects of composite foam beams under macroscopic bending" section of the Supplementary Materials, shown in fig. S4), the foam adapts to various deformation modes such as body motion, tides, winds, and vibrations to convert various mechanical energies into electricity without complicated mechanisms and abrasion caused by moving parts.

Other dielectric materials such as degradable polymers and even natural materials also exhibit the flexoelectric effect. They can make biodegradable or biocompatible omnidirectional electromechanical sensors and generators. Therefore, this work breaks the limitation of low flexoelectric effect of solids at the macroscale and paves a way for wide applications of flexoelectricity.

MATERIALS AND METHODS
Fabrication
PDMS prepolymer (SYLGARD 184A) and a thermal curing agent (SYLGARD 184B) were mixed at a weight ratio of 10:1, and the mixture was denoted as "precured PDMS." CCTO particles (shown in fig. S5A) were fully mixed with the precured PDMS at a specific mass ratio, and the bubbles were removed by leaving the mixture in vacuum for 30 min. Here, NaCl particles were selected as the sacrificial template at a specific mass ratio (the details are given in the Calculation of mass ratio section of Materials and Methods), which were vigorously stirred with the precured PDMS/CCTO mixture. The mixture was then injected into a mold [cross section, 2 cm by 2 cm; height, 2 mm; and relative twisting angle (θ), 6° between the upper and lower surfaces of the mold]. The mold has a torsional structure printed using a 3D printer (MakerBot PABH65, USA). After curing at 80°C for 60 min, the cured PDMS/CCTO/NaCl composite was submerged in an ultrapure water bath containing an ultrasonic cleaner at 80°C for 72 hours to dissolve the NaCl particles, followed by rinsing five times. The absence of NaCl particles is ensured by measuring the mass of the foam and energy dispersive spectroscopy spectrum, as shown in fig. S5B. After drying in a convection oven (Jinghong DHG-9030A, China) for 2 hours at 80°C, the silver conductive epoxy electrodes (MG Chemicals, 8330S-21G 2-Part Epoxy Kit) with high electric conductivity and low stiffness were brushed on the top surface of the samples. Only the bottom surface of the bottom layer was coated with the electrode. A thin layer of precured PDMS was coated on the top side of the electrode to bond it to the adjacent

layer and to insulate it and cured at 80°C for 1 hour. The twisted PDMS/CCTO foam with a torsional structure (h = 10 mm and θ = 30°) was obtained as the result.

Material characterization
The microscopic structures were characterized by SEM (HITACHI SU8020, Japan), and the microstructure sizes were calculated by averaging the values obtained from ImageJ software.

Experimental setup
The electrostatic charge of the sample was removed by an electrostatic eliminator (KEYENCE SJ-F036, Japan) before each test. A dynamic mechanical analyzer (TA ElectroForce-DMA3200, USA) was used for dynamic loading. A current preamplifier (Stanford Research SR-570, USA) was used to measure and convert the current signal to voltage signal with a low noise gain mode and a low-pass filter method. The real-time voltage signal was recorded by an oscilloscope (Tektronix MDO-3034, USA).

Dielectric permittivity of solid composite
It has been reported that the measured dielectric permittivity of a solid PDMS/CCTO composite agrees with the Yamada model (70), as discussed below (71). Let the dielectric permittivity of the matrix and the filler be ε_1 and ε_2, respectively. Assume that the filler is an ellipsoid with three unequal axes (a, b, c), and the electrostatic field E_x acts on it along the x direction. According to Maxwell equation, the external potential (φ_1) and internal potential (φ_2) at a point (x, y, z) of the ellipsoid are

$$\begin{cases} \varphi_1 = -E_x\left[1 - \dfrac{\varepsilon_2 - \varepsilon_1}{4\pi\varepsilon_1 + (\varepsilon_2 - \varepsilon_1)m^*}\int_a^\infty \dfrac{du}{(a^2 + u)\beta(u)}\right]x \\ \varphi_2 = -E_x\dfrac{4\pi\varepsilon_1}{4\pi\varepsilon_1 + (\varepsilon_2 - \varepsilon_1)m^*}x \end{cases} \quad (3)$$

where

$$\begin{cases} \dfrac{x^2}{a^2+a} + \dfrac{y^2}{b^2+a} + \dfrac{z^2}{c^2+a} = 1 \\ \beta(u) = \dfrac{\sqrt{(a^2+u)(b^2+u)(c^2+u)}}{2\pi abc} \\ m^* = \int_a^\infty \dfrac{du}{(a^2+u)\beta(u)} \end{cases} \quad (4)$$

Let the dielectric permittivity of an infinitesimal element Ω of the ellipsoid representing the composite be ε', so the potential ϕ at a point P far away from Ω is as follows

$$\varphi = -E_x\left[1 - \dfrac{\varepsilon' - \varepsilon_1}{4\pi\varepsilon_1 + (\varepsilon - \varepsilon_1)m^*}\dfrac{V}{r^3}\right]x \quad (5)$$

where V is the volume of Ω and r is the distance from P to Ω. Assuming that Ω contains N filler ellipsoids, the potential at P can be obtained as follows

$$\varphi = -E_x\left[1 - N\dfrac{\varepsilon_2 - \varepsilon_1}{4\pi\varepsilon_1 + (\varepsilon_2 - \varepsilon_1)m^*}\dfrac{v}{r^3}\right]x \quad (6)$$

The right-hand side of Eq. 5 is equal to that of Eq. 6 so that the dielectric permittivity of the composite ε' can be obtained as

$$\varepsilon' = \varepsilon_1\left[1 + \dfrac{nq(\varepsilon_2 - \varepsilon_1)}{n\varepsilon_1 + (\varepsilon_2 - \varepsilon_1)(1 - q)}\right] \quad (7)$$

where $n = 4\pi/m^*$ is related to the structure of fillers, v is the volume of a filler, and $q = Nv/V$ is the volume fraction of fillers. Figure S1 shows that the dielectric permittivity of the binary composite increases with the dielectric permittivity and volume fraction of the filler.

Calculation of mass ratio

On the basis of the SEM images of the foam structure shown in Fig. 1C, an NaCl particle is assumed to be a cube with the side length l. The volume of each NaCl particle is l^3, and the volume of a unit cell of the foam structure is $(l + x\delta)^3$, where x is a nondimensional parameter related to the geometry of the microstructure; here, $x = 0.5$. According to the definition of mass ratio m, we have

$$m = \frac{m_{\text{NaCl}}}{m_{\text{PDMS}}} \frac{\rho_{\text{NaCl}} \times \left(\frac{l}{\delta}\right)^3}{\rho_{\text{PDMS}} \times \left(\left(\frac{l}{\delta} + \frac{1}{2}\right)^3 - \left(\frac{l}{\delta}\right)^3\right)} \tag{8}$$

where m_{PDMS}, $\rho_{\text{PDMS}} = 1.028$ g/ml, and V_{PDMS} are the mass, density, and volume of PDMS, respectively. m_{NaCL}, $\rho_{\text{NaCL}} = 2.165$ g/ml, and V_{NaCl} are the mass, density, and volume of NaCl particle, respectively. Three values of l/δ are chosen for experiments, namely, 3.5, 4.5, and 6; therefore, m is 4.27, 5.67, and 7.76, which are rounded off to $m = 4$, 6, and 8, respectively.

Flexoelectric output of an ideal microstructured insole

Consider a beam of length l, width, and height δ, whose upper and lower surfaces along l are coated with electrodes. The beam is subjected to three-point bending under the action of a cyclic load F with a frequency $f = 1$ Hz; then, the charge Q induced by the flexoelectric polarization is

$$Q = \frac{\mu_{1133} F \delta l^2}{8EI^*} = \mu_{1133} l \varepsilon_{11}^{\max} \tag{9}$$

where E, I^*, μ_{1133}, and $\varepsilon_{11}^{\max}$ are the elastic modulus, the moment of inertia of the section, the transverse flexoelectric coefficient, and the maximum strain of the middle cross section of the beam, respectively . Assume that the macroscopic bottom surface area and height of a porous insole are S and h, respectively, and the insole is uniformly compressed during walking so that the internal ligaments undergo the same deformation. All of the surfaces with the same polarity are connected in series; then, the total amount of polarized charge Q_{sum} generated by the insole is

$$Q_{\text{sum}} = nQ = \frac{4Shl\mu_{1133}\varepsilon_{11}^{\max}}{\delta(1+\delta)^2} \tag{10}$$

where $n = 4Sh/\delta (l + \delta)^2$ is the total number of ligaments inside the porous insole. If for example, $S = 200$ cm^2, $h = 1$ cm, $l = 2.25$ μm, $\delta = 0.5$ μm, $\mu_{1133} = 4.5 \times 10^{-9}$ C/m, $\varepsilon_{11}^{\max} = 0.5$, then $Q_{\text{sum}} = 1.08$ C.

During walking, the peak current I and peak voltage U of the insole are $I = 2\pi f Q_{\text{sum}} = 6.78$ A and $U = 10$ V. After being rectified by a rectifier, the peak current, peak voltage, and instantaneous power generated by a pair of insoles connected in parallel are 13.6 A, 10 V, and 136 W. The charge generated in one load cycle (period, $T = 1$ s) is Q_1

$$Q_1 = 2\int_0^{\frac{T}{2}} I dt = 2\int_0^{\frac{T}{2}} 13.6 \sin 6.28t \, dt = 8.6 \text{ C} \tag{11}$$

Therefore, to fully charge the batteries of 4000 and 400 mA·hour by a pair of insoles, it will only take 27 min and 167 s, respectively.

Supplementary Materials

This PDF file includes:
Supplementary Text
Figs. S1 to S5

Other Supplementary Material for this manuscript includes the following:
Movies S1 and S2

REFERENCES AND NOTES

1. S. M. Kogan, Piezoelectric effect during inhomogeneous deformation and acoustic scattering of carriers in crystals. *Sov. Phys. Solid State* **5**, 2069–2070 (1964).
2. P.-G. De Gennes, J. Prost, *The Physics of Liquid Crystals* (Oxford Univ. Press, 1993).
3. S. Krichen, P. Sharma, Flexoelectricity: A perspective on an unusual electromechanical coupling. *J. Appl. Mech.* **83**, 030801 (2016).
4. L. Shu, R. Liang, Z. Rao, L. Fei, S. Ke, Y. Wang, Flexoelectric materials and their related applications: A focused review. *J. Adv. Ceram.* **8**, 153–173 (2019).
5. L. Molina-Luna, S. Wang, Y. Pivak, A. Zintler, H. H. Pérez-Garza, R. G. Spruit, Q. Xu, M. Yi, B. X. Xu, M. Acosta, Enabling nanoscale flexoelectricity at extreme temperature by tuning cation diffusion. *Nat. Commun.* **9**, 4445 (2018).
6. S. Baskaran, X. He, Y. Wang, J. Y. Fu, Strain gradient induced electric polarization in α-phase polyvinylidene fluoride films under bending conditions. *J. Appl. Phys.* **111**, 014109 (2012).
7. B. Chu, D. R. Salem, Flexoelectricity in several thermoplastic and thermosetting polymers. *Appl. Phys. Lett.* **101**, 103905 (2012).
8. M. Zhang, D. Yan, J. Wang, L. H. Shao, Ultrahigh flexoelectric effect of 3D interconnected porous polymers: Modelling and verification. *J. Mech. Phys. Solids* **151**, 104396 (2021).
9. M. Grasinger, K. Mozaffari, P. Sharma, Flexoelectricity in soft elastomers and the molecular mechanisms underpinning the design and emergence of giant flexoelectricity. *Proc. Natl. Acad. Sci. U.S.A.* **118**, e2102477118 (2021).
10. A. G. Petrov, Electricity and mechanics of biomembrane systems: Flexoelectricity in living membranes. *Anal. Chim. Acta* **568**, 70–83 (2006).
11. Q. Deng, L. Liu, P. Sharma, Flexoelectricity in soft materials and biological membranes. *J. Mech. Phys. Solids* **62**, 209–227 (2014).
12. F. Ahmadpoor, P. Sharma, Flexoelectricity in two-dimensional crystalline and biological membranes. *Nanoscale* **7**, 16555–16570 (2015).
13. F. Vasquez-Sancho, A. Abdollahi, D. Damjanovic, G. Catalan, Flexoelectricity in bones. *Adv. Mater.* **30**, 1705316 (2018).
14. R. Meyer, Piezoelectric effects in liquid crystals. *Phys. Rev. Lett.* **22**, 918–921 (1969).
15. J. Harden, B. Mbanga, N. Iber, K. Fodor-Csorba, S. Sprunt, J. T. Gleeson, A. Jákli, Giant flexoelectricity of bent-core nematic liquid crystals. *Phys. Rev. Lett.* **97**, 157802 (2006).
16. J. Narvaez, F. Vasquez-Sancho, G. Catalan, Enhanced flexoelectric-like response in oxide semiconductors. *Nature* **538**, 219–221 (2016).
17. R. Mbarki, N. Baccam, K. Dayal, P. Sharma, Piezoelectricity above the Curie temperature? Combining flexoelectricity and functional grading to enable high-temperature electromechanical coupling. *Appl. Phys. Lett.* **104**, 122904 (2014).
18. L. Wang, S. Liu, X. Feng, C. Zhang, L. Zhu, J. Zhai, Y. Qin, Z. L. Wang, Flexoelectronics of centrosymmetric semiconductors. *Nat. Nanotechnol.* **15**, 661–667 (2020).
19. Z. Wang, X. X. Zhang, X. Wang, W. Yue, J. Li, J. Miao, W. Zhu, Giant flexoelectric polarization in a micromachined ferroelectric diaphragm. *Adv. Funct. Mater.* **23**, 124–132 (2013).
20. A. Abdollahi, I. Arias, Constructive and destructive interplay between piezoelectricity and flexoelectricity in flexural sensors and actuators. *J. Appl. Mech.* **82**, 121003 (2015).
21. U. K. Bhaskar, N. Banerjee, A. Abdollahi, Z. Wang, D. G. Schlom, G. Rijnders, G. Catalan, A flexoelectric microelectromechanical system on silicon. *Nat. Nanotechnol.* **11**, 263–266 (2016).
22. L. Shu, S. Ke, L. Fei, W. Huang, Z. Wang, J. Gong, X. Jiang, L. Wang, F. Li, S. Lei, Z. Rao, Y. Zhou, R. K. Zheng, X. Yao, Y. Wang, M. Stengel, G. Catalan, Photoflexoelectric effect in halide perovskites. *Nat. Mater.* **19**, 605–609 (2020).
23. S. M. Park, B. Wang, S. Das, S. C. Chae, J. S. Chung, J. G. Yoon, L. Q. Chen, S. M. Yang, T. W. Noh, Selective control of multiple ferroelectric switching pathways using a trailing flexoelectric field. *Nat. Nanotechnol.* **13**, 366–370 (2018).
24. X. Jiang, W. Huang, S. Zhang, Flexoelectric nano-generator: Materials, structures and devices. *Nano Energy* **2**, 1079–1092 (2013).

25. H. Zhang, B. Chu, Energy harvesting by exploiting the enhanced flexoelectric-like response of reduced $(Na_{0.5}Bi_{0.5})_{0.92}Ba_{0.08}TiO_3$ ceramics. *J. Eur. Ceram. Soc.* **38**, 2520–2525 (2018).

26. Q. Deng, M. Kammoun, A. Erturk, P. Sharma, Nanoscale flexoelectric energy harvesting. *Int. J. Solids Struct.* **51**, 3218–3225 (2014).

27. K. Chu, B. K. Jang, J. H. Sung, Y. A. Shin, E. S. Lee, K. Song, J. H. Lee, C. S. Woo, S. J. Kim, S. Y. Choi, T. Y. Koo, Y. H. Kim, S. H. Oh, M. H. Jo, C. H. Yang, Enhancement of the anisotropic photocurrent in ferroelectric oxides by strain gradients. *Nat. Nanotechnol.* **10**, 972–979 (2015).

28. J. Jiang, Z. Chen, Y. Hu, Y. Xiang, L. Zhang, Y. Wang, G. C. Wang, J. Shi, Flexo-photovoltaic effect in MoS_2. *Nat. Nanotechnol.* **16**, 894–901 (2021).

29. R. Guo, L. You, W. Lin, A. Abdelsamie, X. Shu, G. Zhou, S. Chen, L. Liu, X. Yan, J. Wang, J. Chen, Continuously controllable photoconductance in freestanding $BiFeO_3$ by the macroscopic flexoelectric effect. *Nat. Commun.* **11**, 2571 (2020).

30. M. M. Yang, A. N. Iqbal, J. J. P. Peters, A. M. Sanchez, M. Alexe, Strain-gradient mediated local conduction in strained bismuth ferrite films. *Nat. Commun.* **10**, 2791 (2019).

31. B. Wang, Y. Gu, S. Zhang, L. Q. Chen, Flexoelectricity in solids: Progress, challenges, and perspectives. *Prog. Mater. Sci.* **106**, 100570 (2019).

32. M. Yang, D. J. Kim, M. Alexe, Flexo-photovoltaic effect. *Science* **360**, 904–907 (2018).

33. H. Lu, C. W. Bark, D. Esque De Los Ojos, J. Alcala, C. B. Eom, G. Catalan, A. Gruverman, Mechanical writing of ferroelectric polarization. *Science* **336**, 59–61 (2012).

34. S. M. Park, B. Wang, L.-Q. Chen, T. W. Noh, S. M. Yang, D. Lee, Flexoelectric control of physical properties by atomic force microscopy. *Appl. Phys. Rev.* **8**, 041327 (2021).

35. D. Lee, A. Yoon, S. Y. Jang, J. G. Yoon, J. S. Chung, M. Kim, J. F. Scott, T. W. Noh, Giant flexoelectric effect in ferroelectric epitaxial thin films. *Phys. Rev. Lett.* **107**, 057602 (2011).

36. G. Catalan, A. Lubk, A. H. G. Vlooswijk, E. Snoeck, C. Magen, A. Janssens, G. Rispens, G. Rijnders, D. H. A. Blank, B. Noheda, Flexoelectric rotation of polarization in ferroelectric thin films. *Nat. Mater.* **10**, 963–967 (2011).

37. L. J. McGilly, A. Kerelsky, N. R. Finney, K. Shapovalov, E. M. Shih, A. Ghiotto, Y. Zeng, S. L. Moore, W. Wu, Y. Bai, K. Watanabe, T. Taniguchi, M. Stengel, L. Zhou, J. Hone, X. Zhu, D. N. Basov, C. Dean, C. E. Dreyer, A. N. Pasupathy, Visualization of moiré superlattices. *Nat. Nanotechnol.* **15**, 580–584 (2020).

38. Y. Li, X. Wang, D. Tang, X. Wang, K. Watanabe, T. Taniguchi, D. R. Gamelin, D. H. Cobden, M. Yankowitz, X. Xu, J. Li, Unraveling strain gradient induced electromechanical coupling in twisted double bilayer graphene moiré superlattices. *Adv. Mater.* **33**, 2105879 (2021).

39. R. Maranganti, N. D. Sharma, P. Sharma, Electromechanical coupling in nonpiezoelectric materials due to nanoscale nonlocal size effects: Green's function solutions and embedded inclusions. *Phys. Rev. B Condens. Matter Mater. Phys.* **74**, 014110 (2006).

40. R. Maranganti, P. Sharma, Atomistic determination of flexoelectric properties of crystalline dielectrics. *Phys. Rev. B Condens. Matter Mater. Phys.* **80**, 054109 (2009).

41. P. Zubko, G. Catalan, A. K. Tagantsev, Flexoelectric effect in solids. *Annu. Rev. Mat. Res.* **43**, 387–421 (2013).

42. X. Wen, D. Li, K. Tan, Q. Deng, S. Shen, Flexoelectret: An electret with a tunable flexoelectriclike response. *Phys. Rev. Lett.* **122**, 148001 (2019).

43. R. A. Awang, T. Baum, K. J. Berean, P. Yi, K. Kalantar-Zadeh, S. Sriram, W. S. T. Rowe, Elastomeric composites for flexible microwave substrates. *J. Appl. Phys.* **119**, 124109 (2016).

44. M. Ahmadipour, M. F. Ain, Z. A. Ahmad, A short review on copper calcium titanate (CCTO) electroceramic: Synthesis, dielectric properties, film deposition, and sensing application. *Nano-Micro Lett.* **8**, 291–311 (2016).

45. D. C. Sinclair, T. B. Adams, F. D. Morrison, A. R. West, $CaCu_3Ti_4O_{12}$: One-step internal barrier layer capacitor. *Appl. Phys. Lett.* **80**, 2153–2155 (2002).

46. M. Li, D. C. Sinclair, A. R. West, Extrinsic origins of the apparent relaxorlike behavior in $CaCu_3Ti_4O_{12}$ ceramics at high temperatures: A cautionary tale. *J. Appl. Phys.* **109**, 084106 (2011).

47. L. Gibson, M. Ashby, *Cellular Solids: Structure and Properties* (Cambridge University Press, 1988), vol. 9.

48. P. Zubko, G. Catalan, A. Buckley, P. R. L. Welche, J. F. Scott, Strain-gradient-induced polarization in $SrTiO_3$ single crystals. *Phys. Rev. Lett.* **99**, 167601 (2007).

49. J. Gao, H. Cao, X. Hu, H. Mao, X. Chen, M. Qiu, H. Verweij, Y. Fan, Piezoelectric porous α-quartz membrane by aqueous gel-casting with enhanced antifouling and mechanical properties. *J. Eur. Ceram. Soc.* **43**, 109–120 (2023).

50. Z. G. Zuo, F. R. Ling, D. Li, J. S. Liu, J. Q. Yao, The effect of electric field on the dielectric permittivity of BST/STO superlattice. *Mod. Phys. Lett. B* **27**, 1350066 (2013).

51. C. Sevik, C. Bulutay, Theoretical study of the insulating oxides and nitrides: SiO_2, GeO_2, Al_2O_3, Si_3N_4, and Ge_3N_4. *J. Mater. Sci.* **42**, 6555–6565 (2007).

52. N. R. Harris, M. Hill, R. Torah, R. Townsend, S. Beeby, N. M. White, J. Ding, A multilayer thick-film PZT actuator for MEMs applications. *Sens. Actuat. A Phys.* **132**, 311–316 (2006).

53. L. Gu, J. Liu, N. Cui, Q. Xu, T. Du, L. Zhang, Z. Wang, C. Long, Y. Qin, Enhancing the current density of a piezoelectric nanogenerator using a three-dimensional intercalation electrode. *Nat. Commun.* **11**, 1030 (2020).

54. D. Zhu, S. Beeby, J. Tudor, N. White, N. Harris, Improving output power of piezoelectric energy harvesters using multilayer structures. *Procedia Eng.* **25**, 199–202 (2011).

55. R. Sriramdas, S. Chiplunkar, R. M. Cuduvally, R. Pratap, Performance enhancement of piezoelectric energy harvesters using multilayer and multistep beam configurations. *IEEE Sens. J.* **15**, 3338–3348 (2015).

56. S. R. Kwon, W. B. Huang, S. J. Zhang, F. G. Yuan, X. N. Jiang, Flexoelectric sensing using a multilayered barium strontium titanate structure. *Smart Mater. Struct.* **22**, 115017 (2013).

57. S. Zhang, F. Li, X. Jiang, J. Kim, J. Luo, X. Geng, Advantages and challenges of relaxor-$PbTiO_3$ ferroelectric crystals for electroacoustic transducers – A review. *Prog. Mater. Sci.* **68**, 1–66 (2015).

58. Y. M. You, W. Q. Liao, D. Zhao, H. Y. Ye, Y. Zhang, Q. Zhou, X. Niu, J. Wang, P. F. Li, D. W. Fu, Z. Wang, S. Gao, K. Yang, J. M. Liu, J. Li, Y. Yan, R. G. Xiong, An organic-inorganic perovskite ferroelectric with large piezoelectric response. *Science* **357**, 306–309 (2017).

59. T. Zheng, H. Wu, Y. Yuan, X. Lv, Q. Li, T. Men, C. Zhao, D. Xiao, J. Wu, K. Wang, J. F. Li, Y. Gu, J. Zhu, S. J. Pennycook, The structural origin of enhanced piezoelectric performance and stability in lead free ceramics. *Energ. Environ. Sci.* **10**, 528–537 (2017).

60. D. Xue, Y. Zhou, H. Bao, C. Zhou, J. Gao, X. Ren, Elastic, piezoelectric, and dielectric properties of $Ba(Zr_{0.2}Ti_{0.8})O_3-50(Ba_{0.7}Ca_{0.3})TiO_3$ Pb-free ceramic at the morphotropic phase boundary. *J. Appl. Phys.* **109**, 054110 (2011).

61. K. Xu, J. Li, X. Lv, J. Wu, X. Zhang, D. Xiao, J. Zhu, Superior piezoelectric properties in potassium–sodium niobate lead-free ceramics. *Adv. Mater.* **28**, 8519–8523 (2016).

62. H. Tao, H. Wu, Y. Liu, Y. Zhang, J. Wu, F. Li, X. Lyu, C. Zhao, D. Xiao, J. Zhu, S. J. Pennycook, Ultrahigh performance in lead-free piezoceramics utilizing a relaxor slush polar state with multiphase coexistence. *J. Am. Chem. Soc.* **141**, 13987–13994 (2019).

63. P. Li, J. Zhai, B. Shen, S. Zhang, X. Li, F. Zhu, X. Zhang, Ultrahigh piezoelectric properties in textured (K,Na)NbO_3-based lead-free ceramics. *Adv. Mater.* **30**, 1705171 (2018).

64. F. Li, D. Lin, Z. Chen, Z. Cheng, J. Wang, C. Li, Z. Xu, Q. Huang, X. Liao, L. Q. Chen, T. R. Shrout, S. Zhang, Ultrahigh piezoelectricity in ferroelectric ceramics by design. *Nat. Mater.* **17**, 349–354 (2018).

65. J. Cao, C. Rendon Piedrahita, Z. Zhao, B. D. Vogt, T. Kyu, Tuning flexoelectric effect in polymer electrolyte membranes via cation selection for potential energy harvesting applications. *ACS Appl. Energy Mater.* **3**, 328–335 (2020).

66. Z. L. Wang, J. Song, Piezoelectric nanogenerators based on zinc oxide nanowire arrays. *Science* **312**, 242–246 (2006).

67. J. Sun, H. Guo, G. N. Schädli, K. Tu, S. Schär, F. W. M. R. Schwarze, G. Panzarasa, J. Ribera, I. Burgert, Enhanced mechanical energy conversion with selectively decayed wood. *Sci. Adv.* **7**, eabd9138 (2021).

68. F. Yi, X. Wang, S. Niu, S. Li, Y. Yin, K. Dai, G. Zhang, L. Lin, Z. Wen, H. Guo, J. Wang, M. H. Yeh, Y. Zi, Q. Liao, Z. You, Y. Zhang, Z. L. Wang, A highly shape-adaptive, stretchable design based on conductive liquid for energy harvesting and self-powered biomechanical monitoring. *Sci. Adv.* **2**, e1501624 (2016).

69. D. Liu, X. Yin, H. Guo, L. Zhou, X. Li, C. Zhang, J. Wang, Z. L. Wang, A constant current triboelectric nanogenerator arising from electrostatic breakdown. *Sci. Adv.* **5**, eaav6437 (2019).

70. G. Liu, Y. Chen, M. Gong, X. Liu, Z. K. Cui, Q. Pei, J. Gu, C. Huang, Q. Zhuang, Enhanced dielectric performance of PDMS-based three-phase percolative nanocomposite films incorporating a high dielectric constant ceramic and conductive multi-walled carbon nanotubes. *J. Mater. Chem. C* **6**, 10829–10837 (2018).

71. T. Yamada, T. Ueda, T. Kitayama, Piezoelectricity of a high-content lead zirconate titanate/polymer composite. *J. Appl. Phys.* **53**, 4328–4332 (1982).